Probabilistic data association based on intersection of Orbit Sets

Laura Pirovano
Surrey Space Centre, University of Surrey, l.pirovano@surrey.ac.uk

Daniele Antonio Santeramo
Aerospace Department, Politecnico di Milano, danieleantonio.santeramo@polimi.it

Roberto Armellin
Surrey Space Centre, University of Surrey, r.armellin@surrey.ac.uk

Pierluigi di Lizia
Aerospace Department, Politecnico di Milano, pierluigi.dilizia@polimi.it

Alexander Wittig
University of Southampton, a.wittig@soton.ac.uk

ABSTRACT

Untraced space debris are the principal threat to the functioning of operational satellites whose services have become a fundamental part of our daily life. Small debris between 1 and 10 cm are currently too small to be cataloged and are only detectable for a limited amount of time when surveying the sky. The very-short arc nature of the observations makes it very difficult to perform precise orbit determination with only one passage of the object over the observing station. For this reason the problem of data association becomes relevant: one has to find more observations of the same resident space object to precisely determine its orbit. This paper is going to illustrate a novel approach that exploits Differential Algebra to handle the data association problem in a completely analytical way. The paper presents an algorithm that uses the Subset Simulation to find correlated observations starting from the solution to the Initial Orbit Determination problem. Due to the different capabilities of the observatories, several observing strategies are currently being used. The algorithm is thus tested for different strategies against a well known approach from literature. Then, the performance of the data association method is tested on some real observations obtained in two consecutive nights. Finally, preliminary results for data association without Initial Orbit Determination are shown.

1. INTRODUCTION

The problem of determining the state of resident space objects (RSOs) is fundamental to maintain a collision-free environment in space, predict space events and perform activities. Due to the development of new technologies and the ever-growing number of RSOs, the number of observations available is increasing by the day. This calls for more efficient methods able to deal with the amount of data produced. Furthermore, when surveying the sky, the short-arc nature of the observations does not allow for precise orbit determination during a single passage of the object over an observing station: being the detections very close in time, little is known about the curvature of the orbit. Thus, for each observation there is more than one orbit that complies with the observation values, as shown in Fig. 1(a). The set of admissible solutions corresponding to a single observational arc is here called the Orbit Set (OS). To reduce the uncertainty on the solution and pinpoint the correct orbit associated with the observation, one needs other independent observations of the same object as sketched in Fig. 1(b). The main challenge in this, however, is to determine whether two or more observations pertain to the same object, thus whether they are correlated, since the objects are unknown when observed. This is the problem of data association, where one has to look for a common solution in the two OSs generated by the observations, as shown in Fig. 1(c) and Fig. 1(d). Current approaches for the data association problem suffer from either high computational effort, due to the point-wise based algorithms to keep high accuracy on the dynamical model, or low accuracy, due to the use of simplified dynamics to keep the problem (semi-)analytical and computationally efficient. This paper proposes an algorithm to perform data association exploiting Differential Algebra (DA) to overcome the issues from literature. DA is a computing technique that uses truncated power series (TPS) instead of numbers to represent variables, thus allowing us to obtain results of complicated functions as high-order Taylor polynomials. For the data association problem, we can thus obtain the definition of the Orbit Set in an analytical form, without the need for point-wise sampling, and propagate the polynomial form in the DA environment independently of the dynamics chosen, thus allowing us to keep accurate dynamics and an analytical description.

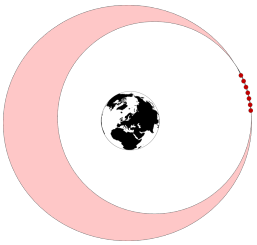

(a) Geometry of the solution for a short-arc observation. The true orbit is contained in a wide range of possible solutions (pink).

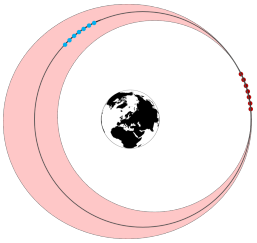

(b) Once other observations of the same object are available, one can pinpoint the true orbit within the uncertainty region (black ellipse).

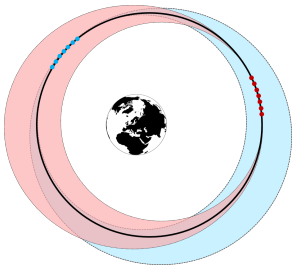

(c) Geometry of correlated observations for short-arc observations. The black orbit is the overlapping solution of the two OSs.

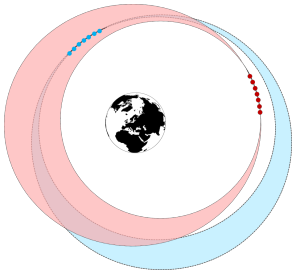

(d) Geometry of uncorrelated observations for short-arc observations: no overlapping solution of the two OSs.

Figure 1: Initial uncertainty region, precise determination of the orbit with new observations of the same object and example of correlated and uncorrelated observations.

In this paper we are focusing on the Initial Value Problem (IVP), that is defining the initial condition of the problem and then propagate it to the next available values. The algorithm developed for this follows three steps. Firstly, an initial orbit determination (IOD) algorithm is developed to compute the state of the orbiting body observed at epoch one. The solution is obtained as a Taylor polynomial that links the uncertainty in the observation to the state of the orbiting body through the use of DA. Some information about DA is given in Section 2.1. Section 2.2 gives a general definition of the DA-IOD algorithm. Secondly, the state computed at epoch one is propagated to a second epoch where a new observation is available. The state is then projected onto the second observation domain, to obtain the observations at the second epoch compatible with the propagated state. Section 2.3 highlights the implementation of the analytical and numerical propagators in the DA environment. At this point, one has an analytical function that maps the observation space at epoch one onto the observation space at epoch two. The third and last step determines the correlation probability of two observation sets, that is the probability that two observations belong to the same object. We make use of the Subset Simulation (SS), a technique that employs Markov Chains Monte Carlo (MCMC) to calculate the probability of rare events. Section 2.4 describes the method and its application to the data association problem. Lastly, Section 2.5 takes a step back and analyzes the possibility to pre-process the observations to reduce the associated uncertainty: here, the steps to perform a linear regression of the observations are shown.
Section 3 shows the results for the DA-IOD algorithm and data association. Firstly, Section 3.1 shows the region of validity of the DA-IOD algorithm by testing it for different observation strategies against the Admissible Region (AR) approach [1, 2]. Section 3.2 shows the accuracy tests for the DA integrator for both analytical and numerical integration. Then, Section 3.3 shows the results for the data association with Subset Simulation performed with real observations taken in two consecutive nights when looking at the Geostationary Earth Orbit (GEO) region. Then, results for the IOD problem are also shown in Section 3.4 for pre-processed data to highlight the possible benefits of the regression. Preliminary results of data association without IOD are also shown. Lastly, Section 4 concludes the paper.

2. MATHEMATICAL BACKGROUND

2.1 DIFFERENTIAL ALGEBRA

This work makes use of DA, a computing technique that uses TPS instead of numbers to represent variables [3]. By substituting the classical implementation of real algebra with the implementation of a new algebra of Taylor polynomials, any deterministic function f of v variables that is C^{k+1} in the domain of interest $[-1,1]^v$ is expanded into its Taylor polynomial up to an arbitrary order k with limited computational effort [4, 5]. The notation for this is: $f \approx \mathcal{T}_f^{(k)}$. Similarly to algorithms for floating point arithmetic, various algorithms were introduced in DA, including methods to perform composition of functions, to invert them, to solve non-linear systems explicitly, and to treat common elementary functions [6]. Ultimately, this technique allows for the definition of analytical solutions of complicated systems of equations which normally require numerical techniques to be solved.
DA variables are defined as follows:

$$[x_0] = x_0 + \delta x_0 \tag{1}$$

where the brackets $[\cdot]$ identify a DA variable, x_0 is the reference value and δx_0 the linear variation with respect to it.

2.2 FIRST STEP: INITIAL ORBIT DETERMINATION

When in survey mode, typical observations in GEO only last a few minutes. Dealing with a very short arc, we are trying to solve the problem of Initial Orbit Determination (IOD). To account for sensor level errors, the precision of the observation (σ_P) can be modeled as white noise and thus be added to the nominal observed values as a Gaussian random variable with zero mean and σ_P standard deviation [7]:

$$\mathbf{Y} \sim \mathcal{N}(\mathbf{y}, \Sigma) \tag{2}$$

where,for the case of optical observations analyzed in this paper, the observed values $\mathbf{y}$ are the right ascension α and the declination δ at three different epochs $(t_{(1,1)}, t_{(1,2)}, t_{(1,3)})$:

$$\mathbf{y}_i = \begin{bmatrix} \alpha_i \\ \delta_i \end{bmatrix}, \quad \text{for } i = 1:3. \tag{3}$$

Assuming independent observations,

$$\Sigma_i = \text{diag}\left(\sigma^2_{P,\alpha_i}, \sigma^2_{P,\delta_i}\right). \tag{4}$$

The DA-IOD algorithm takes as input the observation of an object at three initial epochs $(t_{(1,1)}, t_{(1,2)}, t_{(1,3)})$ and gives as output the TPS of the object state at the central time of the observation $t_{(1,2)}$ expanded with respect to the precision of the observation $\boldsymbol{\sigma_P}$.This is done by initializing the observations as DA variables with the following structure:

$$\begin{cases} [\alpha]_i = \alpha_i + 3\sigma_{P,\alpha_i} \cdot \delta\alpha_i \\ [\delta]_i = \delta_i + 3\sigma_{P,\delta_i} \cdot \delta\delta_i \end{cases} \qquad \text{for: } i = 1:3 \tag{5}$$

thus defining a 6 dimensional uncertainty domain through the use of the 99.7% confidence interval for Gaussian variables. In this way we obtain an analytical map that describes the relationship between the state of the satellite and the uncertainty input. In particular, the map is:

$$f_{IOD} = \mathcal{T}^{(k)} : (\boldsymbol{\alpha}_{t_1}, \boldsymbol{\delta}_{t_1}) \subset \mathbb{R}^6 \rightarrow (\boldsymbol{r}_{t_1}, \boldsymbol{v}_{t_1}) \subset \mathbb{R}^6. \tag{6}$$

For varying values of the input within the confidence interval, one can find the state of the body by means of a simple function evaluation. The algorithm makes use of Gauss's solution as first guess for the ranges ρ_1, ρ_2, ρ_3 and refines it by imposing continuity for the velocity at $t_{(1,2)}$ by exploiting the solutions of the Lambert's algorithm from $t_{(1,1)}$ to $t_{(1,2)}$ and from $t_{(1,2)}$ to $t_{(1,3)}$. A simple sketch of the method is shown in Fig. 2, while details of the mathematical description can be found in [8].

Due to the polynomial form of the solution, the region of validity is determined by tolerance set on the truncation error, which defines a *convergence region*. This implies that in general, one single TPS may not able to describe the entire OS. The Automatic Domain Splitting (ADS) tool [9, 10, 11] is thus applied to the DA-IOD algorithm to estimate the truncation error and control it: when the truncation error exceeds the tolerance, the ADS automatically splits the initial $(\boldsymbol{\alpha}, \boldsymbol{\delta})$-domain into sub-regions and calculates a new TPS over the new subdomain. The ADS needs two input parameters: the truncation tolerance and the maximum number of splits. With this division, the solution is described as a list of TPS that accurately describe the state of the observed body over the entire initial domain. The updated form of the map with the ADS notation is:

$$f_{IOD+ADS} = \bigcup_i \mathcal{T}_i^{(k)} : (\boldsymbol{\alpha}_{t_1}, \boldsymbol{\delta}_{t_1})_i \subset \mathbb{R}^6 \rightarrow \left(\boldsymbol{r}_{t_{(1,2)}}, \boldsymbol{v}_{t_{(1,2)}}\right)_i \subset \mathbb{R}^6. \tag{7}$$

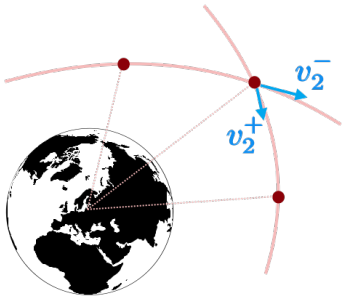

(a) Gauss: first guess for the ranges. They don't define a unique orbit and the velocity vector is discontinuous at the central time of observation.

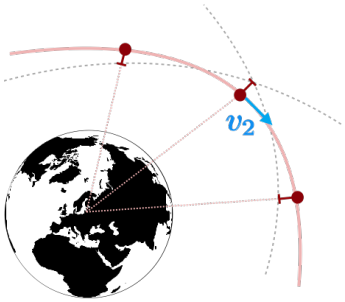

(b) Lambert: continuity for the velocity is imposed to find the correction for the ranges. On e unique orbit is defined for the nominal observations.

Figure 2: Sketch of the DA-IOD algorithm.

Fig. 3 shows an application of the ADS to the Gaussian function by plotting the absolute error between the polynomial approximation and the exact form with and without ADS. Fig. 3(a) shows the exact function, while in Fig. 3(b) the sub-domains used to approximate it are superimposed. Fig. 3(c) and Fig. 3(d) show the absolute error between the exact function and the polynomial approximation. It is clear that in Fig. 3(c) the error grows unbounded, while setting a tolerance, in this case 10^{-5} forces the ADS to split the domain into 64 sub-domains and respect the threshold in the entire domain. The ADS thus ensures the accuracy of the map over the entire domain considered.

The iterative procedure for the computation of the slant ranges within the DA-IOD algorithm may fail if the observation tracklet is too short and/or too uncertain. Indeed, multiple or very poor solutions for the Gauss algorithm fed to the Lambert's algorithm may lead to non-convergence of the iterative procedure to refine the solution and produce hyperbolic orbits. This may happen both during the calculation of the point solution or during the calculation of the expansion map in case a small portion of it fall within an hyperbolic area. In the latter case, only a point value is available. This possibility is discussed in Section 3.1.

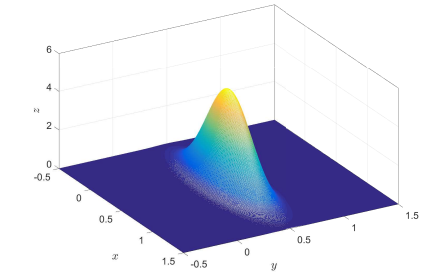

(a) Gaussian function: one polynomial approximates the entire domain.

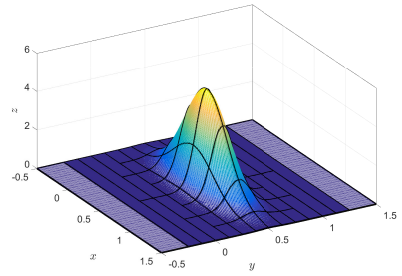

(b) Gaussian function divided into patches: each patch is a polynomial approximation.

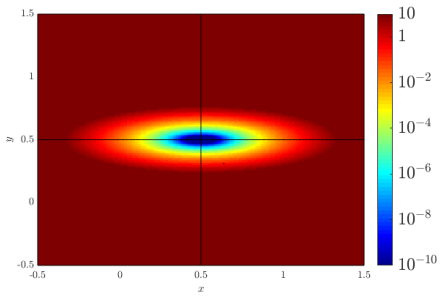

(c) Absolute error without ADS.

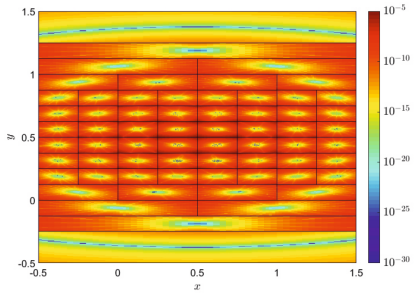

(d) Absolute error with ADS.

Figure 3: Example of ADS applied to Gaussian function [8].

2.3 SECOND STEP: PROPAGATION

Once the state of the satellite is found at $t_{(1,2)}$, one needs to propagate it to a second epoch where a new observation is available. The goal is to calculate the function that maps the observation space at the initial epoch into the observation space at the second epoch, to find whether the propagated observations intersect the real ones and thus correlation can be found. The main feature of the integrator developed is its ability to work with both DA and ADS. Indeed, due to the non-linear nature of the propagation, the truncation error is expected to grow and thus further splitting is necessary during the integration process to keep an accurate map.

Two different integrators are presented and their accuracy checked in this paper: the analytical Keplerian integrator and the numerical propagator. The first one has been developed to solve the two-body problem and is used throughout this paper. The second integrator represents a further step in the development of an algorithm to accurately propagate the OSs and analyze the influence of perturbations on the data association.

The main advantage of having a DA propagator is the possibility to integrate an uncertainty cloud in polynomial

form and then access the value of a single point just by means of a function evaluation. In Section 3.2 the integrators are tested against MATLAB numerical integrator to check the accuracy of the cloud integration against the point-wise integration.

2.4 THIRD STEP: DATA ASSOCIATION

The IOD solution is associated with a rather large uncertainty due to the short nature of the observations, which is further increased when propagated. This implies that the uncertainty of the map projected onto the observation plane at the second epoch $(\hat{\boldsymbol{\alpha}}_{t_2}, \hat{\boldsymbol{\delta}}_{t_2})$ is significantly larger with respect to the uncertainty of the actual observations $(\boldsymbol{\alpha}_{t_2}, \boldsymbol{\delta}_{t_2})$. The intersection of the two volumes can thus be regarded as rare event and algorithms optimized for the calculation of small failure probabilities such as the Subset Simulation (SS) can be used.

2.4.1 Subset Simulation theory

The probability of an event defined over a continuous probability density function (PDF) can be generally calculated as [12]:

$$p_I = \int 1_I(\theta)\pi(\theta)d\theta, \tag{8}$$

where $\theta \in \mathbb{R}^d$ represents the uncertain parameter, $\pi(\theta)$ is the joint PDF for θ, $I \subset \mathbb{R}^d$ is the intersection domain and 1_I is the indicator function of the intersection domain:

$$\begin{cases} 1_I = 1 & \text{if } \theta \in I \\ 1_I = 0 & \text{if } \theta \notin I \end{cases}. \tag{9}$$

The original and best known stochastic simulation algorithm for estimating high-dimensional integrals is Monte Carlo Simulation (MCS). In this method the probability p_I is estimated by approximating the indicator function by its mean over N sample events:

$$p_I \approx p_I^{MC} = \frac{1}{N}\sum_{i=1}^{N} 1_I\left(\theta^{(i)}\right). \tag{10}$$

However, MCS has a serious drawback: it is inefficient in estimating rare events probabilities. Indeed when p_I is very small ($p_I << 1$), one requires a big number of samples $N \propto p_I^{-1} >> 1$ to accurately estimate p_I. This is where the SS comes into play: the basic idea of SS [13] is to represent a very small probability as a product of larger probabilities, calculated sequentially. Starting from the initial domain, that is $\mathbb{R}^d$, one can find a sequence of nested sub-domain that shrink up until the intersection domain I, called *failure domain* in literature due to its initial use to calculate failure probabilities: $\mathbb{R}^6 \supset I_0 \supset I_1 \supset I_{j-1} \supset I_j = I$. The intersection probability p_I can then be calculated as the product of conditional probabilities at previous levels:

$$p_I = \prod_{k=1}^{j} P(I_k \mid I_{k-1}). \tag{11}$$

Clearly, by choosing the intermediate failure domains appropriately, all conditional probabilities p_k can be made large and the original problem be replaced by k intermediate ones. In particular, we implement the Modified Metropolis algorithm, described in detail in [12]. Here, the main steps are reported. The algorithm starts with a MCS of the initial domain. The sampling is performed according to the distribution $\pi(\theta)$. To define the intermediate domains, a specific positive-valued function $g : \mathbb{R}^d \to \mathbb{R}$ also called *performance function* is used: $g(\theta)$ may represent some a behavior that rarely happens for a threshold b. The domain I can thus be defined as

$$I = \left\{\theta \in \mathbb{R}^d \mid g(\theta) < b\right\}, \tag{12}$$

and the intermediate sub-regions as

$$I_j = \left\{\theta \in \mathbb{R}^d \mid g(\theta) < b_j\right\}, \tag{13}$$

where the intermediate thresholds satisfy the constraint $b_0 > b_1 > \ldots > b_{m-1} > b_m = b$. Intermediate threshold values b_j define the values of the conditional probabilities $p_j = P(F_j|F_{j-1})$ and, therefore, affect the efficiency of the SS. In practical cases the b_j are chosen adaptively so that the estimated conditional probabilities are equal to a fixed value $p_0 = 0.1$. In specific, after ranking the N samples according to their performance g, the coefficient b_j is chosen as

$$b_j = \frac{g\left(\theta^{(Np_0)}\right) + g\left(\theta^{(Np_0+1)}\right)}{2} \tag{14}$$

so that the best performing Np_0 points are accepted and the conditional probability satisfied. For each accepted sample at level 0, a MCMC is then built: after performing a random walk with variance σ_W^2, the proposed candidate $\tilde{\xi}$ is checked against the seed through the initial probability distribution $\pi(\cdot)$ by calculating the acceptance ratio for each component k of the vector

$$r_k = \frac{\pi_k\left(\tilde{\xi}_k\right)}{\pi_k\left(\theta_k^{(i)}\right)}. \tag{15}$$

$\tilde{\xi}_k$ is accepted only if it passes a uniform test with parameter $\min(1, r)$. Once the Np_0 chains are calculated, they are ranked again and the process is continued until the intermediate tolerance b_j falls below the final tolerance b. Fig. 4 shows the process for $N = 10$ and $p_0 = 0.1$. The dark red dots are the initial 10 MCS, then only the best performing sample ($Np_0 = 1$) is kept and a new chain (red) is calculated to re-fill the population. The new 10 points at Level 1 are then ranked and filtered with the tolerance b_1. The second level marks the last step because $b_2 < b$. Considering the conditional probability at each sub-level has been fixed as p_0, the rare probability of the event can be calculated as:

$$p_I = \prod_{j=1}^{m-1}(p_0) \cdot \frac{N_m}{N} \tag{16}$$

where m is the number of sub-regions and N_m is the number of samples that fall within the I_m region.

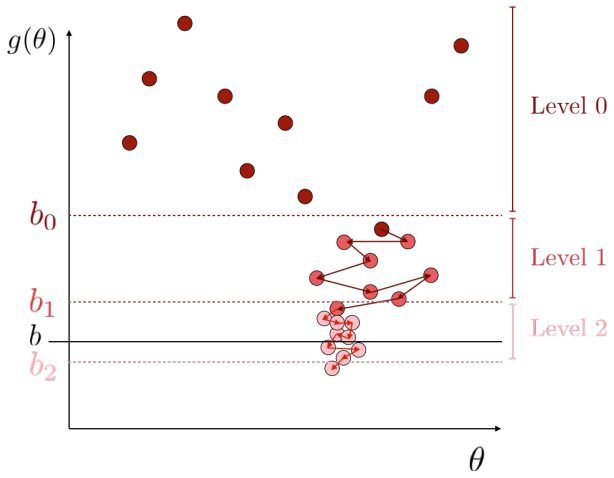

Figure 4: Sketch of the Subset Simulation algorithm with Markov Chains Monte Carlo. $N = 10$ initial samples and $p_0 = 0.1$ conditional probability.

2.4.2 Subset Simulation for data association

The SS can be applied to the data association problem to find the small intersection between the uncertainty volume of the observation at the second epoch and the observation map propagated from the first epoch. Fig. 5 shows the passages that lead to the calculation of the intersection volume: thanks to the use of DA, we have an analytical function that maps Observation 1 onto Observation 2 (depicted as the dotted pipe, which increases its uncertainty when propagated in time). The map goes from $\mathbb{R}^6$ to $\mathbb{R}^6$ through the calculation of the IOD solution, propagation and projection:

$$f = \bigcup_i \mathcal{T}_i^{(k)} : (\boldsymbol{\alpha}_{t_1}, \boldsymbol{\delta}_{t_1}) \subset \mathbb{R}^6 \rightarrow (\boldsymbol{\alpha}_{t_2}, \boldsymbol{\delta}_{t_2}) \subset \mathbb{R}^6. \tag{17}$$

The function f is a union of i polynomials of order k created with the ADS.

The SS then looks for the values $(\boldsymbol{\alpha}_{t_1}, \boldsymbol{\delta}_{t_1})$ that are mapped into Observation 2 domain (thin pipe). The parameter θ is Observation 1, with associated probability

$$\pi(\theta) = \mathcal{N}(\boldsymbol{\mu}, \Sigma) \tag{18}$$

where the mean $\boldsymbol{\mu}$ is defined in Eq. 3 and the covariance matrix Σ in Eq. 4. The sampling of $(\boldsymbol{\alpha}_{t_1}, \boldsymbol{\delta}_{t_1})$ and subsequent calculation of IOD, propagation and projection is thus just a function evaluation.

Having considered the uncertainty on the observation as white noise as detailed in Eq. 18, the sum of the residuals is again a well known probabilistic distribution:

$$J = \sum_{i=1}^{3} \left[\left(\frac{\hat{\alpha}_i - \alpha_{t_{(2,i)}}}{\sigma_{(2,i)}} \right)^2 + \left(\frac{\hat{\delta}_i - \delta_{t_{(2,i)}}}{\sigma_{(2,i)}} \right)^2 \right] \sim \chi^2 \,(6) \tag{19}$$

where $\hat{\boldsymbol{\alpha}}$ and $\hat{\boldsymbol{\delta}}$ are the calculated observations through f, while $(\boldsymbol{\alpha}_{t_2}, \boldsymbol{\delta}_{t_2})$ and $\boldsymbol{\sigma}_2$ are respectively the new observations and their precision. The residual function can thus be modeled as a chi-square and can be used as performance function to rank the samples during the SS: the smaller the residuals are, the closer the samples are to being in the intersection volume.

The final threshold b is chosen as the quantile of the χ^2 of level α = 0.003 and order 6:

$$q_{\chi^2(0.003,6)} = 19.8 \tag{20}$$

having six observed parameters and being $3\boldsymbol{\sigma}_2$ the $3-\sigma$ variation of a Gaussian distribution.

The key for a fast convergence is the adaptive choice of the variance σ_W^2 for the random walk to build the MCMCs. Indeed, if the variance is left unchanged from the initial MCS, at further levels the step may be too large and each proposed candidate $\tilde{\xi}$ rejected, or too small and the migration of the samples slow. To optimize the convergence, the variance is thus updated such that the acceptance of new candidates falls within 30% and 50% [12].

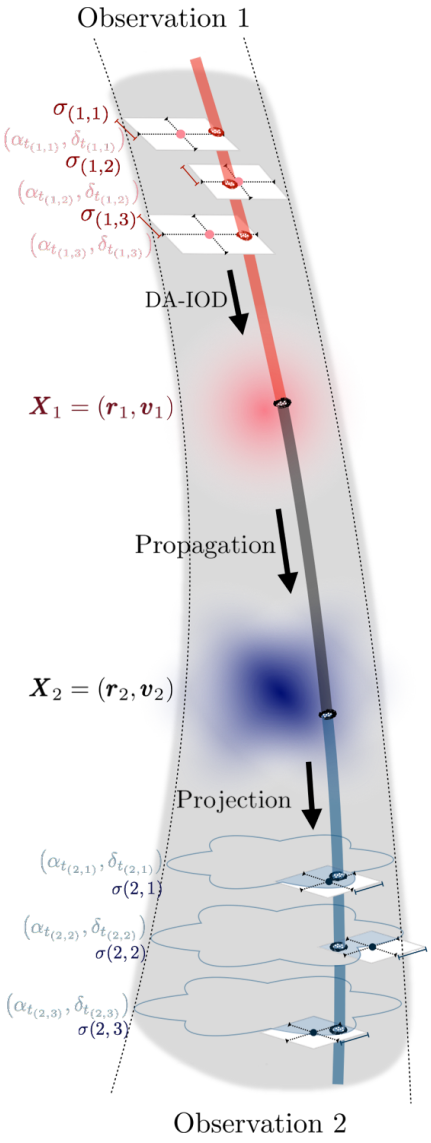

Figure 5: Sketch of the algorithm for data association: connecting DA-IOD (Red), propagation (black), projection (blue) with associated uncertainty (large pipe). Then, exploiting SS to find the intersection volume and estimate correlation (thin pipe).

2.5 STATISTICAL ANALYSIS OF OBSERVATIONS

So far, we have considered only three observations out of the entire tracklet (first, middle and last) to gather the most information about the curvature of the orbit. However, typical observing strategies include more than 3 observations; this means we have disregarded other observed parameters which could give more insight on the orbit of the observed body. If more than three observations are available for a very short tracklet, the distribution of the right ascension and declination can be linearly regressed with respect to time, following the well known linear regression equation $\hat{\boldsymbol{Y}} = \hat{\boldsymbol{\beta}}_0 + \hat{\boldsymbol{\beta}}_1 \boldsymbol{X}$:

$$\begin{bmatrix} \hat{\alpha} \\ \hat{\delta} \end{bmatrix} = \begin{bmatrix} \hat{\alpha}_0 \\ \hat{\delta}_0 \end{bmatrix} + \begin{bmatrix} \dot{\hat{\alpha}} \\ \dot{\hat{\delta}} \end{bmatrix} t \tag{21}$$

This can be conveniently done at the central time of observation (C). The resulting values $(\hat{\alpha}_C, \hat{\delta}_C, \dot{\hat{\alpha}}, \dot{\hat{\delta}})$ are known as *Attributable*, from the well known AR approach. The quantity

$$T = \frac{\hat{\beta} - \beta}{s_{\hat{\beta}}} \sim t_{N-2} \tag{22}$$

is known to be distributed as a T-Student [14], where $\hat{\beta}$ stands for any of the 4 estimated coefficients that constitute the *Attributable*, N is the number of fitted parameters and $s_{\hat{\beta}}$ is standard estimate (SE) of the coefficient $\hat{\beta}$. Having centered the regression in the central time of observation (thus in the mean value of the predictors), it is trivial to prove that the slope and intercept are uncorrelated. Their variance is thus reduced to being:

$$\Sigma_{Attr} = \mathrm{diag}\left[s_{\hat{\alpha}} \frac{1}{N},\ s_{\hat{\alpha}} \frac{12}{N(N+1)(N-1)\Delta t^2},\ s_{\hat{\delta}} \frac{1}{N},\ s_{\hat{\delta}} \frac{12}{N(N+1)(N-1)\Delta t^2} \right] \tag{23}$$

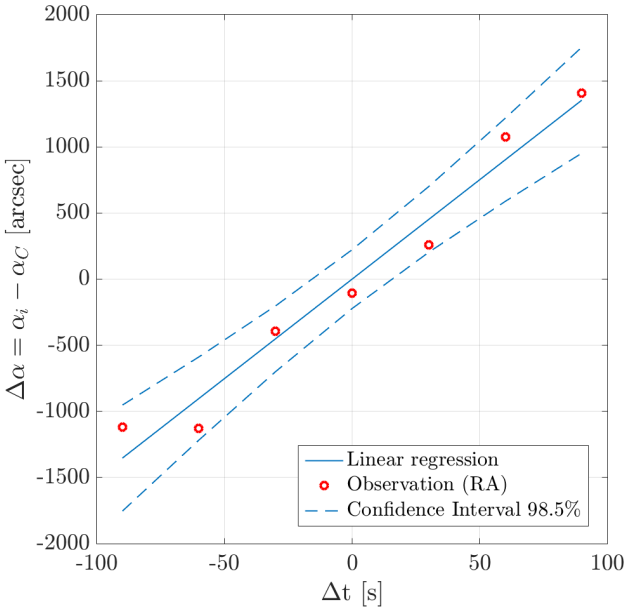

Figure 6: Regression for the right ascension α centered at the central time of observation. Values are amplified by a factor 1000 for clarity purpose.

However, what we are interested in are the interpolated values for the observations and corresponding confidence intervals (CIs), to be able to construct the DA domain as in Eq. 5. Being the predicted values a linear composition of the estimated coefficients, their variance is:

$$\Sigma_{\hat{Y}_i} = H_i \Sigma_{\left(\hat{\beta}_0, \hat{\beta}_1\right)} H_i^T. \tag{24}$$

where $H_i = \begin{bmatrix} 1 & t_i - t_C \end{bmatrix}$. The confidence interval of the predicted observations can then be constructed through $\Sigma_{\hat{Y}_i}$ and the T-Student quantiles:

$$\text{C.I.:} \quad \left[\hat{Y} \pm t_{\frac{\alpha}{2}, n-2} \cdot \sqrt{\text{diag}(\Sigma_{\hat{Y}})} \right] \tag{25}$$

Fig. 6 shows the linear regression for a simulated observation that follows the observing strategy of the ZimSMART telescope [15]: 7 observations each 30 seconds apart, thus constituting a 3 minutes tracklet. Observed values and the CI are amplified by a factor of 1000 to enhance the behavior. The dashed line is the 98.5% confidence interval ($\alpha = 0.03$).

3. RESULTS

3.1 VALIDITY OF DA-IOD ALGORITHM

The DA-IOD algorithm that finds the solution to the IOD problem by expanding the central point with respect to uncertainty in the observation angles is sensitive to two principal variations in the observation: the track length and the uncertainty of the observation. The former contains information about the curvature, thus the shorter the track is, the lesser is known about the curvature of the orbit, increasing the range of possible solutions. The latter directly influences the size of the OS, by defining the uncertainty on the angles, as shown in Eq. 5. So far, the algorithm as been applied to observations retrieved by a specific observatory (TFRM) whose strategy is to observe the object 5 to 8 times every 2 minutes with uncertainty that ranges from 1 to 3 arcsec (considered as the 3σ variation). Although this strategy is shared by other sensors, there is a wide range of different strategies that include shorter, longer, more precise and less precise observations. For this reason the validity of the DA-IOD algorithm had to be tested for different inputs to find the boundary cases that it can handle.

The range for the length of the tracks observed and for the uncertainty were taken from [16] and adapted to also accommodate the strategy adopted by [17, 15]. In particular, when surveying the sky in the GEO region the range for the track length was $[40,\ 3,600]$ s, thus comprising observations that spanned from 0.05% to 4% of the orbital period. The uncertainty spanned $[0.25,\ 50]$ arcsec. The tests have been run on the GEO object with NORAD ID 33595, observed from the TFRM observatory starting on `2016 JAN 11 00:04:47.82`. Each observation was simulated 100 times using the ephemerides of the object created with SPICE [18] and adding white noise. The tracklets comprised three observed values, thus first, middle and last observation identified the entire tracklet and the regression detailed in Section 2.5 was not performed.

Two different outputs need to be analyzed: the point solution for the IOD algorithm and the uncertainty expansion of the map around that point. Fig. 7 shows the success rate for the point solution of the IOD, with a secondary axis showing the arc length in degrees for clarity purpose. There are three macro areas with radically different results: the lower triangle where the algorithm never fails (precise long observations), the upper triangle where the algorithm rarely works (short and very uncertain observations) and the diagonal belt with a success rate around 80 – 90%. The reason for such behavior is the following: the shorter and more uncertain the observation was, the poorer the Gauss' solution

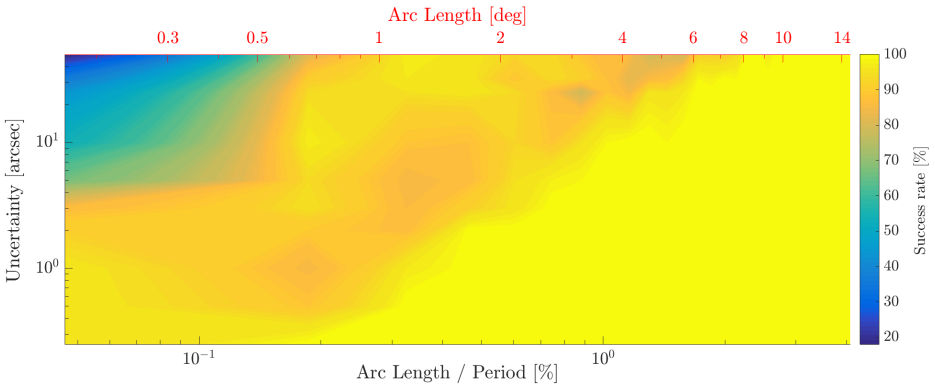

Figure 7: Success rate for point solution of IOD. Three macro areas are found: lower triangle (always success), upper triangle (rare success) and diagonal belt (80 – 90% success).

fed to the Lambert's algorithm was. This led to non convergence of the iterative process to refine the state of the object thus falling within hyperbolic orbits and not allowing for a solution. For boundary values of the observation length and uncertainty, sometimes there was also more than one solution for Gauss's algorithm, this however only happened for initial conditions in the upper triangle. Only when a point solution could be found for the IOD, the expansion map with respect to the uncertainty in the angles was also calculated by exploiting the ADS. Here the initial values contained in the lower triangle and in the diagonal belt in Fig. 7 had very different behaviors. As can be seen in Fig. 8(a), the success rate for the expansion map in diagonal belt is close to zero, while it is always possible to find an expansion map for initial values contained in the lower triangle. The explanation for this very different behavior can be found in Fig. 8(b), where the mean uncertainty of the range ρ is shown: one can see that close to the failure regions the uncertainty grows up until $50,000$ km. A larger uncertainty would trigger hyperbolic solutions and re-entering solutions. This means that where the map expansion fails, the Lambert's algorithm cannot approximate a part of the uncertainty map with elliptic solutions. A clear result in Fig. 8(a) is the presence of a ratio between observation length and uncertainty that determines the feasibility of the DA-IOD algorithm. On Fig. 8(b) two other reference data are shown: the

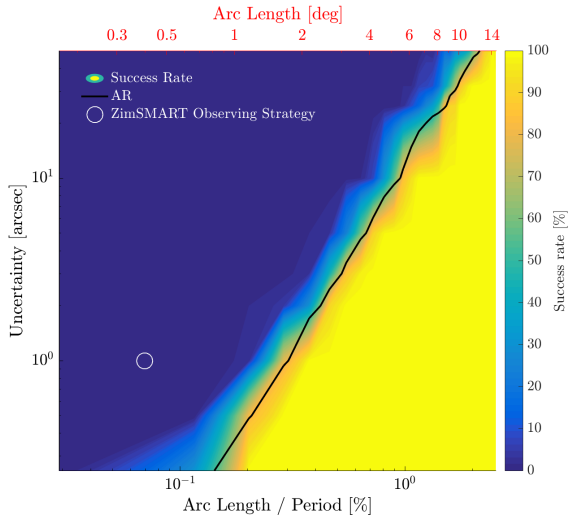

(a) Success rate for the DA-IOD algorithm. There is a net contrast between the area of 100% success and the area of 0% success, thus determining the boundaries of our algorithm. The black line corresponding to the AR is shown for comparison reasons.

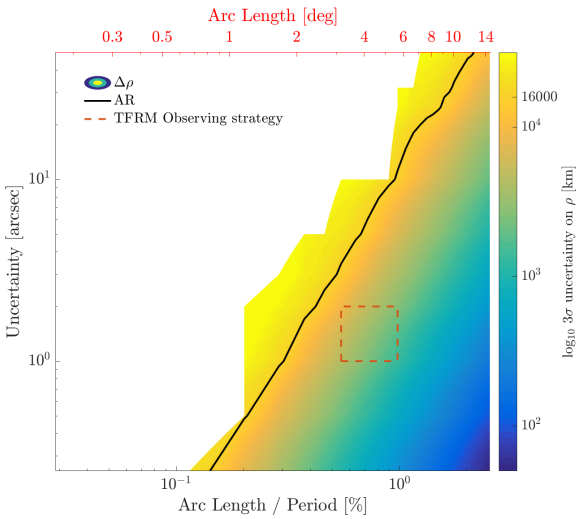

(b) Dimension of the uncertainty over the range for successful runs of the DA-IOD algorithm. Uncertainty for the AR approach is also highlighted (black). The white square represents the initial values considered in this paper, from TFRM approach.

Figure 8: Success rate of DA-IOD algorithm and uncertainty range for ρ for different observation strategies.

red square refers to the typical initial values for observations of the TFRM observatory, which can be easily handled by the algorithm, while the black line ($\Delta\rho \simeq 16,000$ km) is the size of the uncertainty of ρ for the Admissible Region approach [1, 2]. This approach extrapolates four parameters from the observations, leaving two degrees of freedom where the uncertainty is bounded by physical constraints. In specific, the uncertainty over the range was calculated for the following constraints: $a_{min} = 20,000$ km, $a_{max} = 50,000$ km, $e_{max} = 0.75$ km, where the values are respectively minimum semi-major axis, maximum semi-major axis and maximum eccentricity. These constraints comprise both GEO and Geostationary Transfer Orbits (GTOs), which can both be observed when looking at the Geostationary area. Fig. 8 shows that on the boundary of the failure region, our algorithm and the AR have comparable uncertainty on the resulting range. However, the AR is the only viable method for shorter and less precise observations, while, our method can have much smaller uncertainty for longer and more precise observational strategies. This shows that not all observing strategies have to be treated with the AR approach. Some observations contain more information than the attributable and thus can be treated differently to reduce the uncertainty on the output state, as done by the DA-IOD algorithm. The white circle in Fig. 8(a) refers to the strategy adopted by [15] for the ZimSMART telescope. It is easy to check that the DA-IOD algorithm as it is cannot handle this type of strategy. For this reason Section 3.4 analyses the same strategy with pre-processed observations as explained in Section 2.5 to see if the regression can push the boundaries of our algorithm to shorter and more uncertain observations.

3.2 DA-INTEGRATION

To be able to propagate large uncertainties in polynomial form as shown in Fig. 17, one needs an integrator that is able to handle DA variables and the ADS tool. We, thus needed to check the accuracy of the polynomial propagation against point-wise one to ensure that the accuracy of the integration was met on the entire domain propagated. The output of the DA-IOD algorithm described in Section 3.1 is the state of the object in Cartesian Coordinates (CC). However, previous tests showed that propagation carried out with Modified Equinoctial Elements (MEE) was more efficient due to less splits being performed by the ADS. This is explained by the change in the parameters involved: CC all have large variations over one orbital period, while MEE only have one fast varying variable and singularities of classical orbital elements are avoided. Furthermore, in two-body dynamics five out of six MEE parameters remain constant. For this reason, we propagated the state of the body in MEE. Finally, the integrated state was transformed in spherical coordinates due to our need to calculate (α, δ). For this reason we needed to test the accuracy of both the propagation and conversions. The tests were carried out on object NORAD ID 37816 for a 24h integration, with 7^{th} order polynomials. The truncation tolerance for the ADS was set to 10 m for range, 10 m/s for range rate, 10^{-6} rad for right ascension and declination and 10^{-9} rad/s for their variation. Four different checks have been carried out:

- Point-wise numerical integrator in CC against MATLAB numerical integrator: here the implementation of the numerical integrator is tested for point-wise integration before using it with DA variables.
- DA+ADS analytical integrator against point-wise analytical integration: here the map expansion is tested against the point-wise integration with the same analytical integrator, to look at the accuracy of the polynomial form.
- DA+ADS analytical integrator against MATLAB numerical integrator: here the accuracy of the DA analytical integrator is tested against a numerical point-wise integrator.
- DA+ADS numerical integrator in MEE with conversion from CC against MATLAB numerical integrator: here the accuracy of the propagation in MEE starting from the state in CC and ending with the projection on the observation space is tested. This represents the entire process we need for the data association.

Fig. 9 shows the output of a one day integration to give a sense of the uncertainty involved: in Fig. 9(a) the grey line is the real orbit, the grey dots are the centers of the polynomials in CC being propagated, while the yellow and red dots are the centers of the polynomials at final time t_f, respectively for a propagation with MEE and CC. One can see in Fig. 9(b) that the uncertainty on the right ascension spans almost π, while the declination shows a much smaller deviation.

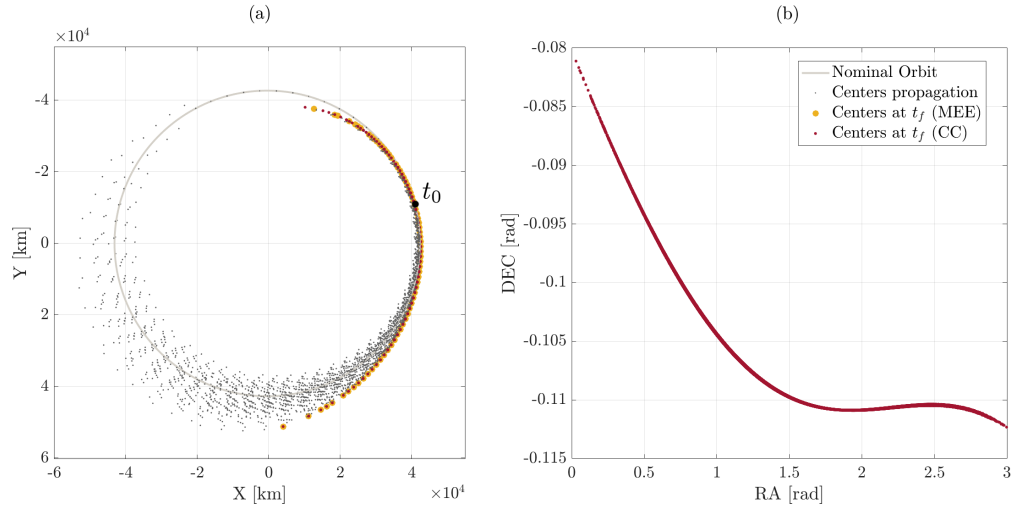

Figure 9: 24h propagation with DA+ADS of a GEO object with focus on the uncertainty on right ascension and declination.

3.2.1 Point-wise numerical integrator in CC against MATLAB numerical integrator

The numerical integrator developed to work with DA and ADS was firstly tested for point-wise integration against the `ode78` MATLAB integrator, which was used for all accuracy tests in this section. All integrations were carried out with an Absolute and Relative tolerance of 10^{-12}. Fig. 10 shows good accordance between the two integrators with a maximum difference in the order of 10^{-9} after 24h propagation. This shows that the numerical integrator developed well integrates the dynamics.

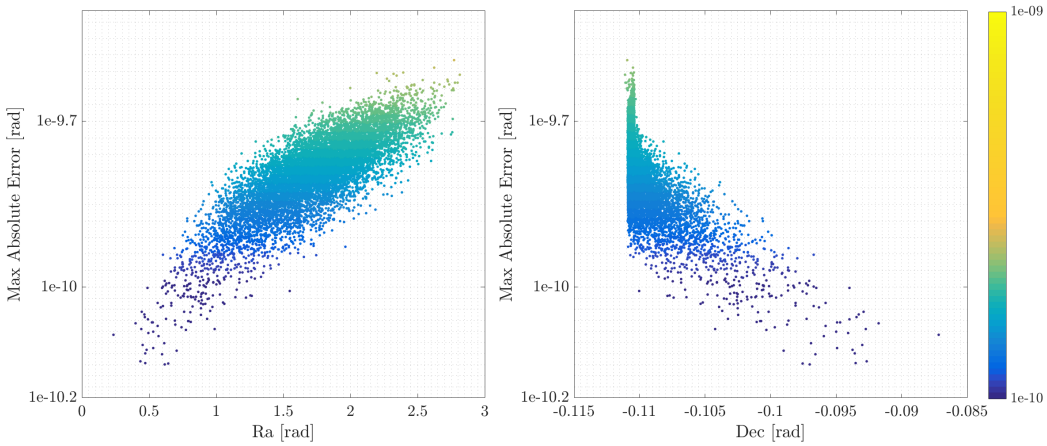

Figure 10: Maximum absolute error on right ascension and declination for point-wise numerical integration against MATLAB integrator.

3.2.2 DA+ADS analytical integrator against point-wise analytical integration

After testing the point-wise integration, the accuracy of the expansion map was tested against point-wise integration with analytical integration. Having set the truncation tolerance to 10^{-6} rad for right ascension and declination, the ADS split the initial domain to enforce it. The absolute error between map evaluation and point-wise integration showed perfect accordance with the tolerance set, thus validating the use of function evaluations of the propagated map for the algorithm developed. One can also appreciate the distribution of the points: it is clear that more sub-domains are needed to well approximate the solutions furthest from the orbital plane (as seen from the declination plot), while the number of domains is evenly distributed on the right ascension plot. Lastly, the error plot is a sum of V-shaped errors:

these are the errors on each sub-domain, smallest at the center and largest at the border.

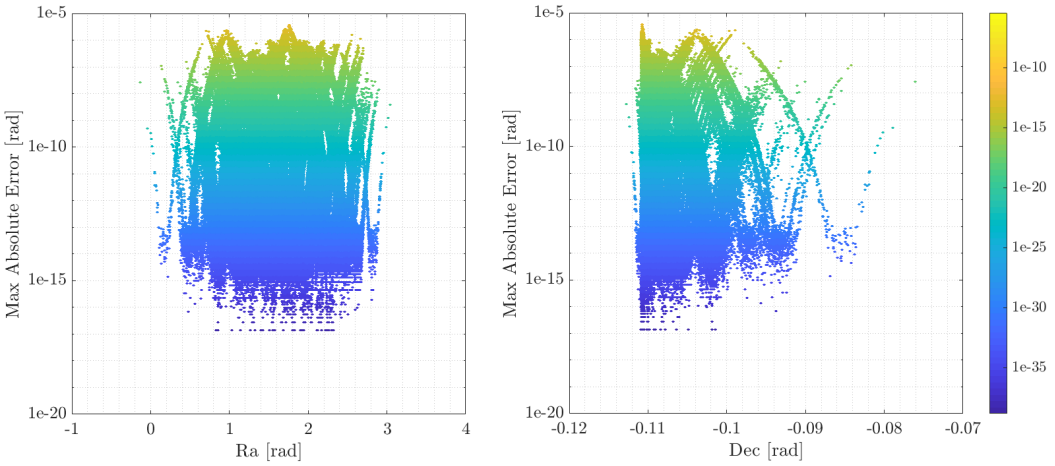

Figure 11: Maximum absolute error on right ascension and declination for map evaluation against point-wise analytical integration.

3.2.3 DA+ADS analytical integrator against MATLAB numerical integrator

After testing the map accuracy against the point-wise analytical integration, the accuracy of the DA integration was checked against MATLAB `ode78` integrator. Having set a tolerance for the ADS of 10^{-6} rad on the angles, the results are in perfect accordance with it, thus proving the good behavior of the propagation with DA. Again, one can appreciate the V-shaped error and the good approximation with few domains of the small declination angles.

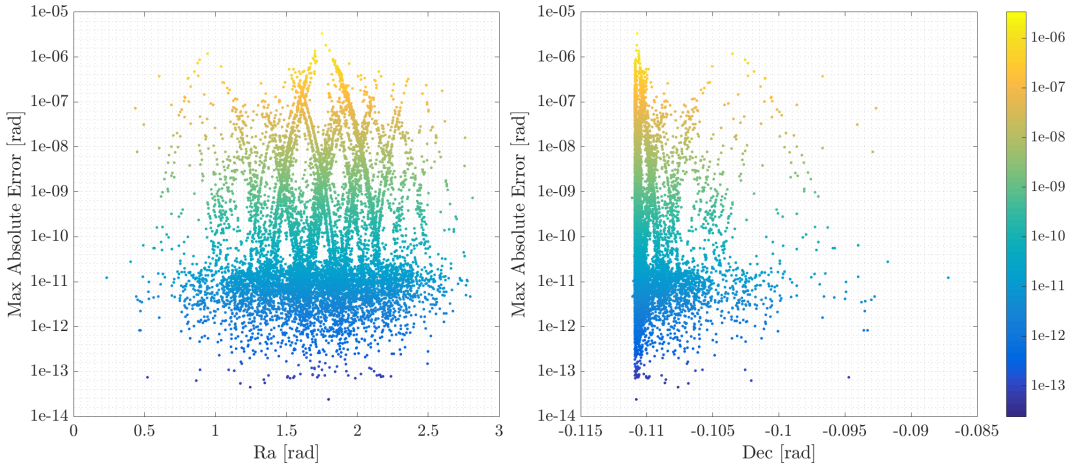

Figure 12: Maximum absolute error on right ascension and declination for DA+ADS analytical integration against MATLAB integrator.

3.2.4 DA+ADS numerical integrator in MEE with conversion from CC against MATLAB numerical integrator

This last test was carried out after validating point-wise and DA integration and DA map evaluation. This checks the entire process needed for data association with SS: the state in CC was transformed to MEE, propagated with DA and projected onto the observation space. This was compared with point-wise numerical integration with MATLAB `ode78`. The results, once again, showed accordance with the tolerances set, proving that the ADS takes care of both conversion and propagation errors during the entire process. One can thus propagate the polynomial found with the DA-IOD algorithm to the epoch where a new observation is found and project it onto the observation space.

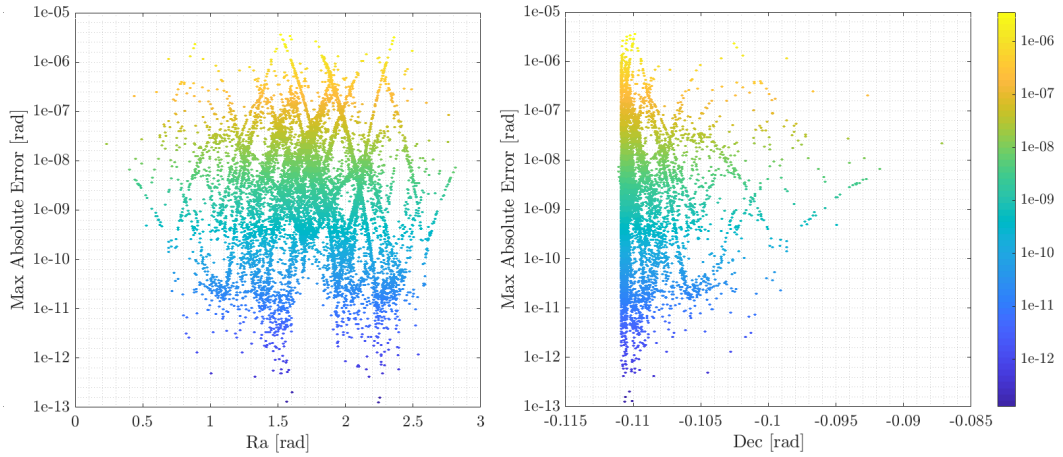

Figure 13: Maximum absolute error on right ascension and declination for MEE map evaluation against point-wise numerical integration.

3.3 DATA ASSOCIATION RESULTS

In this section the results for the data association problem are shown. The DA-IOD algorithm, DA+ADS propagation and SS were put together to solve it. Real observations taken on consecutive nights on January 14 and 15, 2016 from TFRM were used as input. Each tracklet contained between 5 and 8 observations spaced by 2 minutes and with an uncertainty ranging from 1 to 3 arcsec. For each observation, the DA-IOD, DA+ADS Keplerian propagation and SS were run to try to associate observations made around 24h apart. Fig. 14 shows the work of SS over the propagated state. Although the image only shows a 2D area, the algorithm worked at three different observation times simultaneously (thus 6D) to find the values of the first domain that fell withing the acceptance region at the first, middle and last observation times of the second tracklet. As can be noted, the shape of the propagated state in the top plot is the same as in Fig. 9(b). The SS then found the small overlapping domain. This simulation needed five levels to reach convergence and find the correlation. As can be seen, the intersection area is very small and thus a classical MCS would fail in looking for correlation. Furthermore, at each new level one can appreciate the presence of points pertaining to the previous one: these are the best performing values used to create the MCMC at the new Level.

The test case at hand considered 8 observations in two consecutive night and looked for correlation for each one of them. Knowing already which objects the observations pertained to, we were able to assess whether the results of the data association were correct. To avoid processing observations that were

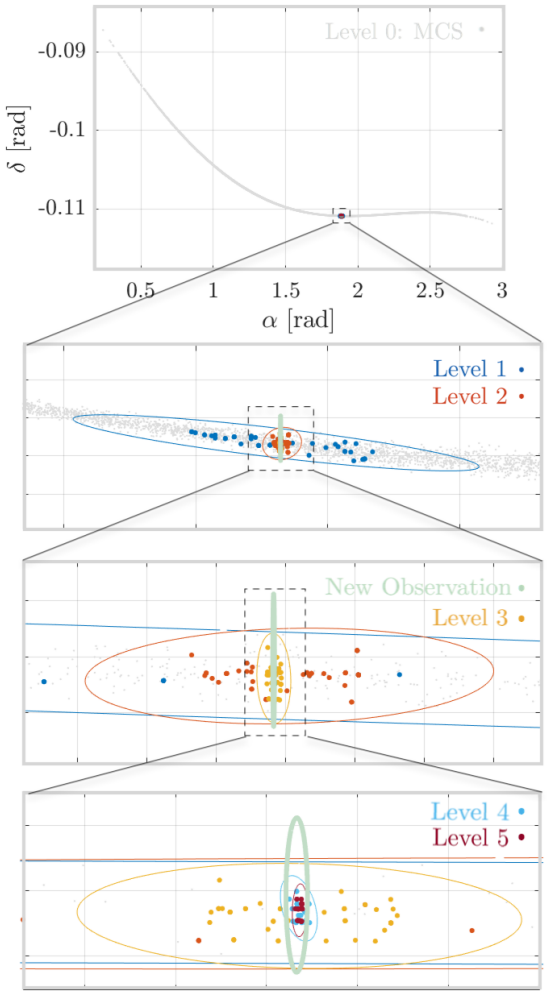

Figure 14: SS for two observations in GEO taken in consecutive nights.

clearly not correlated, an initial check was carried out on the state. The DA-IOD algorithm was performed on both observations considered and the uncertainty over the first five MEE elements calculated: if there was no overlapping, then the observations were discarded without carrying on with the propagation and SS. This could efficiently be done thanks to the `bound` tool implemented in DA which estimates the range of a polynomial over a given domain, thus easily allowing for comparison without the need of point-wise sampling. It has to be noticed that we modified the threshold for correlation b: we indeed multiplied it by an incrementing factor that took into account the error introduced by using Keplerian dynamics. Table 1 shows the results for the correlation carried out on the 64 couples.

Table 1: Results for data association.

		January 14, 2016							
		Obj 1	Obj 2	Obj 3	Obj 4	Obj 5	Obj 6	Obj 7	Obj 8
January 15, 2016	Obj 9	C	T	T	T	T	T	T	T
	Obj 10	C	T	T	T	T	T	T	T
	Obj 11	C	T	T	T	T	T	T	T
	Obj 12	T	SS,FN	T	T	T	T	T	T
	Obj 13	T	T	T	T	C	T	T	T
	Obj 14	T	T	T	T	T	T	C	C
	Obj 15	T	T	T	T	T	T	T	T
	Obj 16	T	T	T	C	T	T	T	T

Legend:

C	Correlated
T	Discarded with test
SS	Discarded after SS
FP	False positive
FN	False Negative.

The table shows that the pre-check on the orbital parameters is able to discard several uncorrelated observations: this saved us from propagating the uncertainty map and performing SS. Although this check was performed on the two-body dynamics hypothesis, other quantities are conserved when the main perturbations are considered: for example the energy and the polar component of the angular momentum are conserved in the zonal problem. We'll thus take into consideration researching into other possible pre-checks, since they make the computation much faster. Once the test was passed correlation was found 7 out of 8 times, with the one non-correlation being a false negative. We believe this was due to the dynamics used: the two-body dynamics may lead to small errors on the computation of the right ascension and declination which determines the false non-correlation, despite the modification of the correlation threshold. Indeed, previous tests carried out on simulated Keplerian observations did not show this behavior, being the dynamics coherent with the data handled. Overall, the method showed good results with only one false negative and no false positive.

3.4 DATA ASSOCIATION WITH PRE-PROCESSED OBSERVATIONS

This section takes a step back to analyze the input of our method. The results for the IOD in Section 3.1 were obtained with raw data. Since our method had 0% success rate for the observing strategy adopted by [15] and depicted in Fig. 8(a) with a white circle, we also ran simulations with pre-processed observations, following the approach defined in Section 2.5.

Table 2: IOD and DA-IOD algorithm with fitted observations for the initial values depicted by the with circle in Fig. 8(a).

Success rate IOD center: 100%		
Confidence Interval	Success rate DA-IOD	$\Delta\rho$
82%	97%	9108 km
90%	42%	17228 km
95%	16%	17580 km
98.5%	2%	18903 km

Indeed, being able to decrease the standard deviation of the fitted parameters through regression we could still be able to solve the DA-IOD problem for shorter and more uncertain initial values. Table 2 summarizes the outcome of the simulations for a 3 min long tracklet made of 7 observations with 1 arcsec uncertainty. First of all, the point solution could always be found, increasing the success rate from 85% to 100%. In the table, the possibility of using larger confidence levels is also contemplated: so fare we've used the $q_{0.997}$ of the Gaussian distribution, but a 5% or 10% confidence level may be enough for our investigation. Clearly, the smaller the confidence we have on the observations, the larger the output uncertainty is, as can be seen from the third column of the Table. It can be noted that, again, when reaching the boundary of the capacity of the DA-IOD algorithm, $\Delta\rho$ gets closer to the size of the AR ($\simeq$ 16000 km). As a result of the size of the uncertainty, the success rate of the DA-IOD

algorithm also drops when the confidence level drops. However, the presence of solutions at all CIs considered hints at the possibility to lower the barrier of the DA-IOD capacity to much shorter tracklets by pre-processing the observation with a linear regression, thus enabling the possibility to handle many more observing strategies with the algorithm proposed with smaller uncertainty associated.

Nevertheless, there are observing strategies for which the DA-IOD algorithm still cannot find a solution. For this region we developed a side algorithm for data association that does not involve the computation of an IOD solution, but uses instead the uncertainty from the AR, which was found to be the best solution for these cases. The main difference, however, is that the attributable too was considered with its own uncertainty. The initial domain was initialized in spherical coordinates, instead of the definition given in Eq. 5. The values for the range and range-rate uncertainty were taken from the AR, the center points ρ_0 and $\dot{\rho}_0$ simply being the mean value:

$$\begin{cases} [\rho] = \rho_0 + \delta\rho \\ [\dot{\rho}] = \dot{\rho}_0 + \delta\dot{\rho} \end{cases} \tag{26}$$

The attributable statistically defined in Section 2.5, had the coefficient estimates as center points and the confidence interval as uncertainty:

$$\begin{cases} [\alpha_C] = \alpha_C + \delta\alpha_C \\ [\dot{\alpha_C}] = \dot{\alpha_C} + \delta\dot{\alpha_C} \\ [\delta_C] = \delta_C + \delta\delta_C \\ [\dot{\delta_C}] = \dot{\delta_C} + \delta\dot{\delta_C} \end{cases} \tag{27}$$

We then tried this approach on the test case presented in [15]: four objects were observed in the same field of view every two hours in a six hours span. Fig. 15 shows the values for the right ascension and declination of the four objects observed.

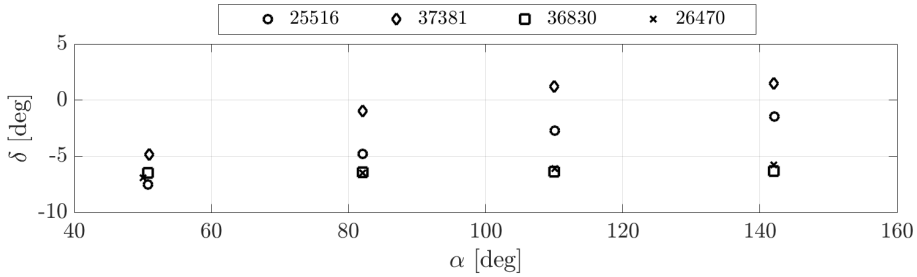

Figure 15: Right ascension and declination of four objects observed four times over a six hours time.

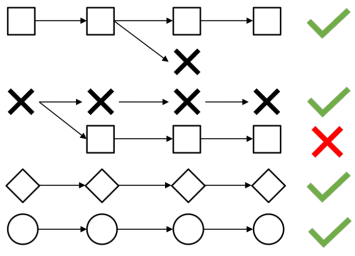

Figure 16: Chains found by the algorithm. Shapes refer to the observations in Fig. 15.

The strategy was the following. Each state observed at t_1 was propagated at t_2 and checked against the new observations. Since the propagation was carried out with the ADS, at each new time step a list of polynomials was available. Each of the polynomials was then checked against the new observations: only if at least one polynomial had a six-dimensional overlapping with the new observations uncertainties, the couple of observations (O_{t_1}, O_{t_2}) was saved. Also in this case, the `bound` tool was exploited to compare the uncertainty ranges. Then, the couples formed were propagated to t_3 where the same check was carried out and the triplets $(O_{t_1}, O_{t_2}, O_{t_3})$ complying were saved. Lastly, the check was performed at t_4 to obtain the full chain $(O_{t_1}, O_{t_2}, O_{t_3}, O_{t_4})$.

Fig. 16 shows the correlations found for the test case presented in Fig. 15: out of 256 possible combinations, the algorithm found 4 true positive, 1 false positive, 0 false negative and 251 true negative. One false correlation was found at t_3 but was then discarded when none of the observations at t_4 was chosen. This triplet was discarded on the

hypothesis that all four objects had been re-observed at all times. We expected a possible false correlation due to the two objects observed (square and cross) having very similar orbital parameters. However, in this particular case the false correlation can be discarded with post-processing, since all other chains contain observations only used once. The algorithm overall looks promising for those observations that do not allow for IOD. However, it would only be suitable for strategies where new observations are acquired after a short amount of time, due to the computational load of propagating a large uncertainty. To give a sense of the size of the propagated domain and underline the use of the ADS in the algorithm, Fig. 17 shows the pruning process of the range and range-rate for the association of the observations of the NORAD ID 36380 object: 4^{th} order polynomials were used, with tolerance of 10 m for the range, 10 m/s for the range rate, 10^{-5} rad for the angles and 10^{-8} for the angle rates.

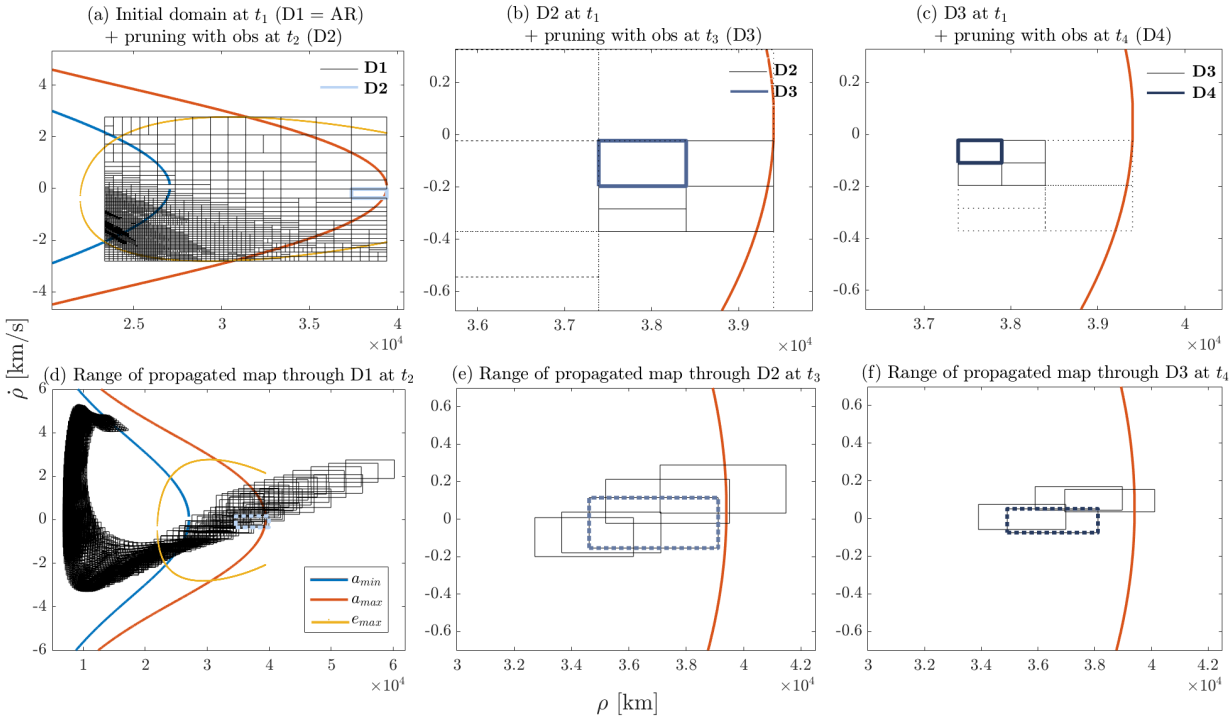

Figure 17: propagation and pruning of intial uncertainty domain.

The initial domain (D1) was initialized with the dimension of the AR, depicted with blue, red and yellow lines in Fig. 17(a). In practice, the AR considered was overestimated to allow for the definition of the domain in a single box. D1 was then propagated with the Keplerian DA+ADS integrator at time t_2. The correspondent $(\rho_2, \dot{\rho}_2)$ uncertainty cloud is shown in Fig. 17(d). Each 6D box of the cloud calculated with the `bound` tool was checked against the uncertainty of the observation at t_2 and only the boxes complying with the constraint of overlapping with the new observation were kept (in this case only one, shown in light blue). The box kept (and shown as D2 in Fig. 17(b)) was then propagated at t_3, where the correspondent $(\rho_3, \dot{\rho}_3)$ uncertainty cloud in Fig. 17(e) was checked against the new observation. Again, only one box was kept (blue box), which served as starting point (D3) in Fig. 17(c) to compute the last pruning (the dark blue box).

4. CONCLUSION

This paper showed a novel method to solve the data association problem. In order to do so, firstly the DA-IOD algorithm was tested to check for which types of observing strategies it was suitable: the test showed that the algorithm was able to obtain a much smaller uncertainty associated to the state with respect to the AR for a certain ratio of length and uncertainty (as for the observations from TFRM). However, the algorithm was not suitable for shorter observations, such as the strategy of the ZimSMART, where the AR was found to be the only viable method. Then the DA+ADS propagator was tested for both Keplerian analytical and numerical integrations. This was necessary to check that the

point-wise integration, the map expansion and the conversions were carried out with the correct accuracy. Tests showed that all of the parts tested were in accordance with the accuracy required. Lastly, the data association was performed. The SS looked for the very small overlapping region between two tracklets only when an initial check on the orbital parameters was positive. This turned out to be a key part of the data association process, since it allowed us to avoid performing propagation and SS for those observations that were clearly non-correlated. The fast check was allowed by the use of a tool developed in DA which estimates the range of polynomial, thus describing the uncertainty regions as boxes, which were efficiently compared. Although results are satisfying, we believe that using Keplerian dynamics may introduce false negatives due to the error introduced on the dynamics, as seen for one case in the results. Having the numerical propagator ready and tested, we'll try to perform the associations considering the main perturbations to check whether these false non-correlations can be avoided. Indeed, we did not see this behavior when dealing with simulated observations in Keplerian dynamics, where the dynamics was coherent with the data handled. Lastly, preliminary results for a data association method that does not involve an IOD solution were presented: indeed, there are some observations for which an IOD is not achievable, thus not allowing for the utilization of the DA-IOD + SS method presented. The new algorithm started from an initial state and uncertainty given from AR and linear regression, thus involving a rather large uncertainty. It then exploited the ADS to perform data association. This method would only be suitable for re-acquisition after a short period, due to the large uncertainty involved. Overall, the results for this new algorithm were rather satisfying with the correct correlation of all four objects and one false positive.

The first step for future work will be the implementation of linear regression to pre-process the observation used for the data association problem. Given the preliminary results on the DA-IOD algorithm shown in this paper, we expect a much faster computation given that a smaller uncertainty will have to be handled. Furthermore, the numerical propagator with the main perturbations will be tested for associations performed over large separations of time. This will check the impact that the dynamics has on the correlation of observations. Furthermore, both methods for data association (with and without IOD) will be tested with more observations to have a better statistics of the correlations. Lastly, the application of the algorithm to boundary value problems (BVP) will also be investigated: being two observations boundary values, there could be ground for improvement in the association approach.

REFERENCES

[1] Andrea Milani, Giovanni Gronchi, Mattia de' Michieli Vitturi, and Zoran Knezevic. Orbit determination with very short arcs. I admissible regions. *Celestial Mechanics and Dynamical Astronomy*, 90(1-2):59–87, 2004.

[2] Andrea Milani and Giovanni Gronchi. *The theory of orbit determination*. 2009.

[3] Roberto Armellin and Pierluigi Di Lizia. Probabilistic initial orbit determination. In *26th AAS/AIAA Space Flight Mechanics Meeting*, pages 1–17, February 2016.

[4] Martin Berz. *The new method of TPSA algebra for the description of beam dynamics to high orders*. Los Alamos National Laboratory, 1986. Technical Report AT-6:ATN-86-16.

[5] Martin Berz. The method of power series tracking for the mathematical description of beam dynamics. *Nuclear Instruments and Methods A258*, 1987.

[6] Martin Berz. *Differential Algebraic Techniques, Entry in Handbook of Accelerator Physics and Engineering*. World Scientific, New York, 1999.

[7] Audrey B Poore, Jeffrey M Aristoff, Joshua T Horwood, Roberto Armellin, William T Cerven, Yang Cheng, Christopher M Cox, Richard S Erwin, Joseph H Frisbee, Matt D Hejduk, Brandon A Jones, Pierluigi Di Lizia, Daniel J Scheeres, David A Vallado, and Ryan M Weisman. Covariance and uncertainty realism in space surveillance and tracking. Technical report, Numerica Corporation Fort Collins United States, 2016.

[8] Laura Pirovano, Daniele Santeramo, Alexander Wittig, Roberto Armellin, and Pierluigi Di Lizia. Initial orbit determination based on propagation of orbit sets with differential algebra. In *7th European Conference on Space Debris, Darmstadt, ESOC*, April 2017.

[9] Alexander Wittig, Pierluigi Di Lizia, Roberto Armellin, Franco Bernelli Zazzera, Kyoko Makino, and Martin Berz. An automatic domain splitting technique to propagate uncertainties in highly nonlinear orbital dynamics. *Advances in the Astronautical Sciences*, 152:1923–1941, 2014.

[10] Alexander Wittig and Roberto Armellin. High order transfer maps for perturbed Keplerian motion. *Celestial Mechanics and Dynamical Astronomy*, pages 1–26, 2015.

[11] Alexander Wittig, Pierluigi Di Lizia, Roberto Armellin, Kyoko Makino, Franco Bernelli-Zazzera, and Martin Berz. Propagation of large uncertainty sets in orbital dynamics by automatic domain splitting. *Celestial Mechanics and Dynamical Astronomy*, 122(3):239–261, 2015.

[12] Konstantin M. Zuev, James L. Beck, Siu-Kui Au, and Lambros S. Katafygiotis. Bayesian post-processor and other enhancements of subset simulation for estimating failure probabilities in high dimensions. *Comput. Struct.*, 92-93:283–296, February 2012.

[13] Siu-Kui Au and James L. Beck. Estimation of small failure probabilities in high dimensions by subset simulation. *Probabilistic Engineering Mechanics*, 16(4):263 – 277, 2001.

[14] George Casella and Roger Berger. *Statistical Inference*. Duxbury Resource Center, June 2001.

[15] M Zittersteijn, A Vananti, T Schildknecht, and V Martinot. A Genetic Algorithm to associate optical measurements and estimate orbits of geocentric objects. In *European Conference for Aerospace Science*, 2015.

[16] Juan Carlos Dolado, Carlos Yanez, and Alfredo Anton. On the Performance Analysis of Initial Orbit Determination Algorithms J.C. Dolado. In *67th International Astronautical Congress (IAC), Guadalajara, Mexico, 26-30 September 2016.*

[17] Jan A. Siminski, Oliver Montenbruck, Hauke Fiedler, and Thomas Schildknecht. Short-arc tracklet association for geostationary objects. *Advances in Space Research*, 53:1184–1194, April 2014.

[18] Navigation and Ancillary Information Facility (NAIF) group. SPICE: An Observation Geometry System for Planetary Science Missions. https://naif.jpl.nasa.gov/naif/index.html. Accessed: 2018-06-13.

ACKNOWLEDGMENTS

We dedicate this work to Javier Montojo who passed away in an accident in Antarctica. Javier supported our research by providing TFRM observations.

The work presented was partlially supported by EOARD and Surrey Space Centre (SSC).